Research Article

Mechanism of tricalcium silicate hydration in the presence of polycarboxylate polymers

Rachel Cook[1] · Hongyan Ma[2] · Aditya Kumar[1]

Abstract

The early-age hydration of cement is inhibited in the presence of comb-shaped polycarboxylate ether (PCE) polymer—a dispersant commonly added to control rheological properties of fresh cement paste. This study employs a series of micro-calorimetry experiments and phase boundary nucleation and growth simulations to elucidate the effects of dosage and molecular architecture of PCE on hydration of tricalcium silicate (Ca_3SiO_5 or C_3S in cement notation), the dominant phase in cement. Results show that PCE—regardless of its molecular architecture—suppresses early-age hydration of C_3S. PCE-induced retardation becomes increasingly more pronounced as dosage of PCE in the paste increases. Such suppression of C_3S hydration has been attributed to adsorption of PCE molecules on silicate surfaces, which inhibit topographical sites of C_3S dissolution and C–S–H nucleation, and impede the post-nucleation growth of C–S–H. This study develops a correlation between molecular architecture of PCE and its ability to suppress C_3S hydration through quantitative analyses of retardation effects induced by PCEs with different molecular architectures. The numerical equation, describing such correlation, offers a reliable, and, more importantly, a readily quantifiable indicator of PCE's potential to suppress C_3S hydration in relation to its dosage and molecular architecture. In the context of practical application of this study, the aforementioned numerical equation can be used to order and rank PCEs—of various molecular architectures—on the bases of their potentials to suppress C_3S hydration, and to select ones that cause the optimum (i.e., user-desired) extent of hydration suppression.

✉ Aditya Kumar, kumarad@mst.edu; Rachel Cook, recwx7@mst.edu; Hongyan Ma, mahon@mst.edu | [1]Department of Materials Science and Engineering, Missouri University of Science and Technology (S&T), B49 McNutt Hall, 1400 N. Bishop, Rolla, MO 65409-0340, USA. [2]Department of Civil, Architectural and Environmental Engineering, Missouri University of Science and Technology (S&T), Rolla, MO 65409-0340, USA.
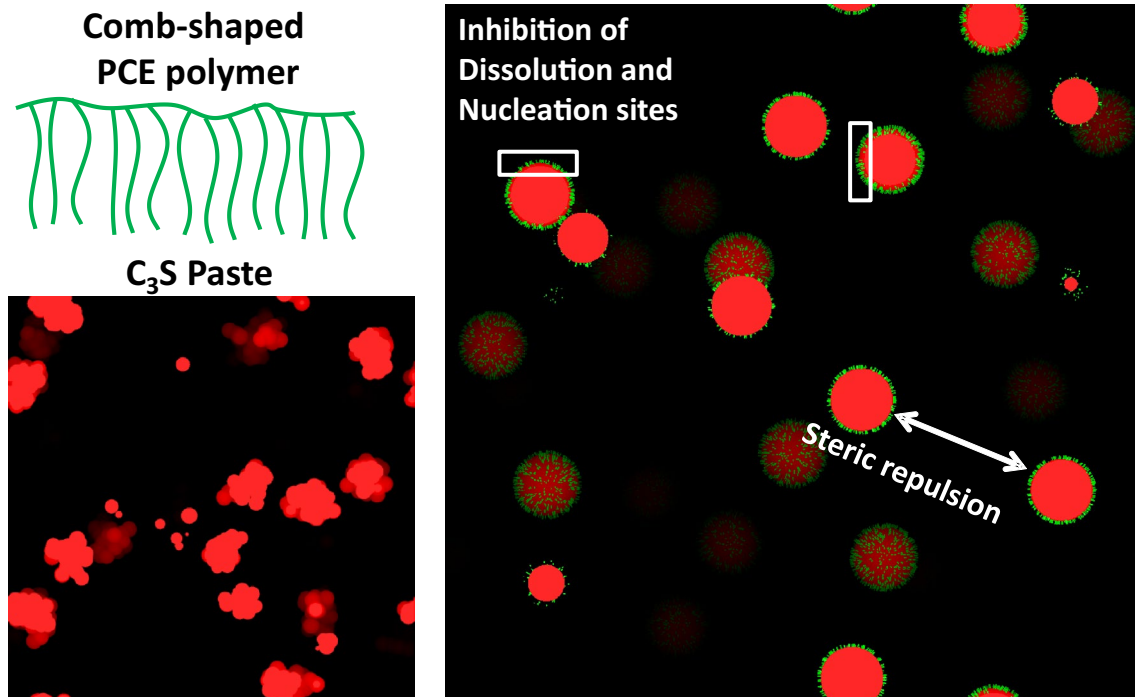
Graphical abstract

1 Introduction

The reaction of cement with water, that is, hydration, involves the occurrence of two concurrent processes—dissolution of anhydrous phases present in cement, and precipitation of hydration products (subsequently referred to as hydrates) [1, 2]. In a typical cement paste (i.e., [cement + water] system), the hydrate that occupies the largest volume fraction—and, thus, considered the main hydrate—is calcium–silicate–hydrate (C–S–H, wherein $C = CaO$, $H = H_2O$, and $S = SiO_2$ as per standard cement notation) [1, 2]. The strong electrostatic bonding between the nanometer-scale components of C–S–H binds the paste cohesively, and lends the solid-to-solid phase connectivity within the paste's microstructure needed for setting and hardening (development of mechanical properties, e.g., compressive strength) [3–6]. In cement pastes, the nucleation of C–S–H occurs in heterogeneous manner on solid substrate boundaries, that is, cement particles' surfaces; as such, the mechanism of its precipitation is typically designated as phase boundary nucleation and growth (pBNG) [3, 7–11]. As properties of cement paste are largely dictated by rate and amount of C–S–H precipitation, factors that affect C–S–H precipitation inevitably affect the development of the paste's mechanical properties. One such factor—that imparts significant effect on C–S–H's nucleation and growth—is the presence of polymer-based chemical admixtures in the paste.

Polycarboxylate ether (PCE) superplasticizers are a well-known class of comb-shaped, polymer-based dispersants, typically used to control the rheological properties of fresh cementitious systems [12, 13] (e.g., high-performance concrete). A singular PCE molecule, if isolated, could be characterized as having comb-shaped architecture, consisting of an anionic backbone—usually formulated using polyacrylic acid or polymethacrylic acid—grafted with a number of hydrophilic ethylene oxide side chains [14–22]. When introduced in cement pastes, PCE's negatively charged backbone adsorb onto positively charged cement particles' surfaces through electrostatic interactions. Meanwhile, the side-chains—which protrude into the solution, oriented away from cement particles' surfaces—induce steric hindrance between neighboring cement particles, thus alleviating the effects of particle agglomeration [14–19]. The plasticizing mechanism of PCE also induces a side-effect—retardation of hydration kinetics of cement [14, 15, 23–25]. More specifically, the adsorption of PCE onto cement particles' surfaces inhibits topographical cement dissolution and C–S–H nucleation sites, thus suppressing cement's reactivity as detailed in the literature [15, 16, 18, 24, 25]. There is consensus among researchers that the molecular architecture of

PCE—specifically, the number of side chains grafted onto each unit of backbone (n), the carboxylate-to-ether ratio (C/E), and the number of ethylene oxide monomers constituting the side chain (P)—significantly affects PCE's adsorption behavior, and, thus, its potential to suppress cement hydration [15–17, 20, 22]. Notwithstanding, the exact mechanisms of PCE-cement interactions, especially in relation to PCE's molecular architecture, are not well understood. Several prior studies have argued that the adsorption capacity of PCE is largely dependent on its side chain grafting density (i.e., inverse of C/E: carboxylate-to-ether ratio), wherein lower grafting densities (or higher C/E) entail higher residual negative charge on the backbone, and, thus, improved adsorption onto positively-charged cement particles' surfaces [15, 26–28]. Other studies, however, have argued that the length of the side chain (i.e., P: number of monomers constituting each side chain)—as opposed to the side chain grafting density—has greater influence on the PCE's adsorption capacity [17, 29]. The premise, here, is that shorter side chains ensure that accessibility to the negative charges on the PCE's backbone is not hindered or limited by steric hindrance (induced by its side chains); this enables better adsorption of PCE molecules onto cement particles' surfaces. In contrast to the above, some studies [15, 16, 30] have posited that the PCE's charge density—which acquires higher values at lower side chain grafting densities (or higher C/E) and shorter side chain lengths (P)—influences the PCE's adsorption capacity the most. More specifically, higher charge density leads to stronger, and better-distributed, electrostatic interactions between cement particles and PCE molecules, and, therefore, improved adsorption. In a recent study, Marchon et al. [22] reported that a more encompassing, composite architectural parameter—that accounts for the aforementioned parameters (i.e., C/E, n, and P) as well as the molecular weight and dosage of PCE in the system—is required to fully describe the effects of PCE on C_3S hydration. The same authors [21] also showed that for a series of cement pastes, provisioned with different dosages of different PCEs, the composite architectural parameter scaled, broadly in a monotonic fashion, with respect to delay in occurrence of the maximum hydration rate. In this study, focus is given to rigorously test the ability of the composite architectural parameter to reliably quantify the retardation caused by PCEs of different molecular architectures.

In addition to aforementioned knowledge gaps—pertaining to correlations between PCE's molecular architecture and its ability to suppress cement hydration—the effect of PCE on nucleation and growth of the main hydrate, i.e., C–S–H, is still not well understood. In recent studies [23, 24, 31], it has been suggested that in cementitious paste provisioned with PCE, due to blockage of nucleation sites by PCE molecules, C–S–H nucleation changes from heterogeneous (i.e., on solid surfaces) to homogeneous (i.e., in the pore space). The authors [23, 24] argued that the change necessitates higher supersaturation for C–S–H precipitation, thus enforcing prolonged dissolution of cement until massive precipitation of C–S–H can occur. However, in other studies [16, 30], it has been shown that while PCE changes the nucleation and growth processes' rate constants (e.g., rate of growth, frequency of nucleation sites), the precipitation of C–S–H still occurs in heterogeneous manner. In a more recent study, Meng et al. [25] argued that even at higher PCE dosages, nucleation and subsequent growth of C–S–H continues to occur heterogeneously, albeit at supressed rates. The authors [25] reported that the suppression is caused by: (1) adsorption of PCE molecules onto cement surfaces—which blocks a fraction of C–S–H nucleation sites, and (2) adsorption of PCE molecules onto C–S–H—which partially blocks C–S–H's access to the pore solution, resulting in the inhibition of its post-nucleation growth.

The above discussion highlights the current state of knowledge, as well as gaps in knowledge, pertaining to underlying mechanisms that link PCE's molecular architecture to its ability to suppress cement hydration and nucleation and growth of C–S–H. The main reason, that would explain these knowledge gaps, is that majority of the past studies have examined the role of PCE in multi-component cementitious systems, in which it is infeasible to de-couple the effects of PCE on dissolution–precipitation hydration process of the two most reactive cement clinker mineral phases, that is, tricalcium silicate (C_3S) and tricalcium aluminate (C_3A, where A: Al_2O_3 as per standard cement notation). For example, in such multi-component cement systems, C_3A hydrates rapidly in the presence of gypsum to form ettringite—which then serves as a favorable adsorbent for PCE molecules [17, 18, 32]. As PCE is drawn in substantial amounts from the solution and adsorbed onto ettringite, the influence of PCE on C_3S hydration rates is marginalized and, therefore, difficult to isolate from the overall response. Furthermore, in multi-component systems, interactions between PCE-and-C_3A and PCE-and-ettringite may affect (i.e., increase or decrease) the amount of free aluminate $[Al(OH)_4]^-$ ions in the solution—which, in turn, makes it difficult to isolate and analyze the net effect of PCE (vis-à-vis that of aluminate ions) on C_3S hydration rates [20, 21]. Therefore, evaluation of such behaviors should be carried out in single-compound systems, which are simpler to analyze than cement but feature the same effects. As noted previously, C_3S is the dominant cement phase (comprising 50–70%$_{mass}$ of cement) [1]. The hydration of C_3S produces two hydrates, that is, C–S–H and CH (portlandite), in stoichiometric quantities, and—like in cement pastes—the nucleation and growth

of C–S–H is the driving mechanism in C_3S pastes. As such, C_3S is deemed a simpler single-compound alternative for cement, and understanding PCE–C_3S interaction can be the basis for understanding PCM–cement interactions.

In this study, a combination of experimental and simulation techniques is used to elucidate the effect of PCE on hydration of C_3S. To fully examine and describe the links between PCE's molecular architecture and its ability to suppress hydration of C_3S, PCEs with three different molecular architectures—albeit, of the same polymer family—are used. The hydration kinetics are monitored, using isothermal microcalorimetry technique, across a broad range of PCE dosages in C_3S pastes. A modified pBNG simulation routine—which has only recently been applied in the literature [11, 25, 33]—is employed to reproduce, and subsequently describe, hydration kinetics of such systems. Focus is given to consolidate results obtained from experiments and simulations, and analyze them in tandem to elucidate the mechanistic origins of PCE-induced suppression of C_3S hydration—including both early and later stages, wherein C_3S hydration is driven by dissolution and nucleation-and-growth, respectively. The mechanisms are ultimately distilled into a single numerical equation that correlates the molecular architecture and dosage of PCE with its potential to influence C_3S hydration kinetics. Such correlation is of significance for practical applications as it can be used as a robust, quantitative basis to compare and rank PCEs on the bases of their potential to suppress C_3S hydration rates, and to select optimum ones based on the type/nature of the application.

Table 1 Architectural parameters of the three PCEs—as determined from SEC-MALS, HPLC, and potentiometric titration techniques [20, 37]

PCE#	C/E	P	n	M_w
PCE-1	1.80	23	20.05	25,145.07
PCE-2	2.10	23	18.10	23,166.84
PCE-3	5.20	17	9.35	11,990.65

Here, C/E (unitless) is the ratio of the number of carboxylate functional groups to the number of ester functional groups, P (unitless) is the number of ethylene oxide monomers per side chain, n (unitless) is the number of side chains per PCE backbone (or the number of repeating units), and M_w (g mol^{-1}) is the calculated molecular weight. M_w is equal to [n. {P. $M_{w,SC}$ + (C/E +1). $M_{w,BB}$}]—wherein, $M_{w,SC}$ (g mol^{-1}) and $M_{w,BB}$ (g mol^{-1}) are the molecular weights of the side chain and backbone, respectively [20, 22]. The nomenclature of the architectural parameters of PCEs was adapted from previous studies [15, 20, 59]

2 Materials and experimental methods

Triclinic C_3S (T_1–Ca_3SiO_5) was synthesized by following a high-temperature synthesis route using phase-pure precursor materials. Calcium oxide (CaO), the residual material left after calcite ($CaCO_3$) decomposition, was mixed with silica (SiO_2, α-quartz) in stoichiometric proportion (CaO:SiO_2 = 3:1), and pelletized at high pressure of 100 MPa. The pellets were then thermally treated in a furnace for 12 h at 1600 °C in platinum receptacles, and subsequently air-quenched [34, 35]. The sintered pellets were then crushed with mortar and pestle, and ground
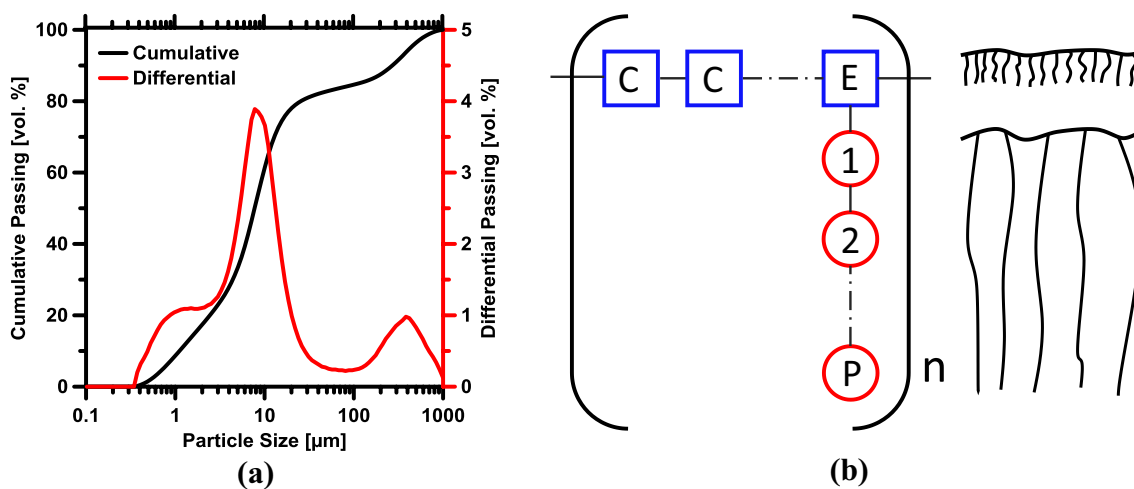

Fig. 1 **a** The cumulative (primary y-axis) and differential (secondary y-axis) particle size distribution (PSD) of C_3S. The largest relative uncertainty in the median diameter (d_{50}, μm) of C_3S, based on six replicate measurements, was on the order of ±6%. **b** Schematic representation of the comb-shaped architecture of PCE, wherein n is the number of repeating units, P is the side chain length, and C/E represents the carboxylate-to-ether ratio

in a ball mill for 24 h. The resulting powder was analyzed via X-ray diffraction (Panalytical X'Pert Pro MPD) and was determined to be C_3S powder containing $\approx 0.80\% \pm 0.20\%$ residual CaO by mass by Rietveld analysis. The particle size distribution (PSD: Fig. 1a) of C_3S was measured using static light scattering analyzer (Microtrac S3500) [36]. The median particle size (d_{50}, μm) of C_3S particulates was determined as 7.78 μm. By combining the PSD of C_3S with its density (i.e., 3150 kg m^{-3}), the specific surface area (SSA_{C3S}) of C_3S particulates was calculated as 562 m^2 kg^{-1}.

Three different polymeric, comb-shaped, PCEs (with solid mass contents of 30%) were used in this study (Fig. 1b). All three PCEs belong to the same polymer family—consisting of polymethacrylic backbone, grafted with polyethylene oxide side chains—albeit their molecular architectures are different. The different PCEs are subsequently referred to as PCE-1, PCE-2, and PCE-3. Details pertaining to the PCEs' molecular architecture, as determined from size exclusion multi-angle light scattering (SEC-MALS), high-performance liquid chromatography (HPLC) and potentiometric titration techniques [20, 37], are listed in Table 1.

Pastes were prepared by mixing deionized-water (DI-water) and C_3S at a constant liquid-to-solid mass ratio (l/s) of 0.45. To describe the role of PCE on C_3S hydration kinetics, the three different PCEs (i.e., PCE-1, PCE-2, and PCE-3, described in Table 1) were added to the pastes at dosages (C_{PCE}) of 0.000, 0.625, 1.250, 1.875, and 2.500% (by mass of C_3S). It is pointed out that these dosages signify the total (i.e., solid + liquid) mass of the PCE. Based on the liquid content of the admixture (i.e., $\approx 30\%_{mass}$ of all PCEs), the aforementioned dosages would amount to 0.000, 0.188, 0.375, 0.563, and 0.750% by solid component of the PCE per unit mass of the binder. The upper bound of dosage, that is, 2.500%, was determined by saturation point test [25, 38] for PCE-1 (with respect to cement paste), and is representative of dosages used in high-performance concretes [13]. The lower dosages of PCE correspond to 25, 50, and 75% of the upper bound, respectively. For provision of PCE into the paste, the mixing-protocol involved mixing of DI-water and PCE for 20 s, followed by an additional minute of mixing with C_3S. For experiments where the upper bound of PCE dosage was employed, PCE was also deployed in delayed mode. Specifically, in delayed mode, a 5-min period, from when the DI-water first came into contact with C_3S, was allowed to elapse before PCE was introduced to the paste. Here, prior to the addition of PCE, the paste was mixed for 1 min, and for another 20 s after PCE was added.

C_3S hydration kinetics in pastes containing approximately 1 g of anhydrous C_3S was monitored for a minimum of 72 h (or 144 h for pastes containing PCE-3), at a constant temperature of 20 °C ± 0.01 °C, using a TAM IV isothermal microcalorimeter. Microcalorimetry techniques are able to monitor heat evolution, resulting from a chemical reaction,

at a high resolution (10^{-8} J s^{-1}). The differential and cumulative heat evolution profiles were divided (or normalized) by the enthalpy of C_3S hydration [1, 35], that is, 484 J g$_{C3S}^{-1}$, to determine the rate of hydration (da/dt, units of h^{-1}) and the degree of hydration (a, reaction mass fraction of C_3S) of C_3S, respectively, as functions of time. The values of a and da/dt calculated in such manner are premised on the assumption that the heat release, determined from microcalorimetry methods, is exclusively due to C_3S hydration. In the context of experiments conducted in this study, the aforementioned assumption is reasonable because the heat release associated with physical and chemical interactions between PCE and C_3S paste components is minuscule compared to heat released from the hydration of C_3S [25, 39].

A thermogravimetric analyzer (TGA, SDT600) was used for identification and quantification of phases present in the binder after 24 h of hydration. Hydration was stopped by crushing the hydrated pastes, into small grains, immersing them in isopropanol for 24 h [40], followed by drying in the oven ($T = 85$ °C) for an additional 24 h. The samples were then ground into fine powder. The powder samples were heated in an inert atmosphere of N_2 over a temperature range of 30–900 °C. The cumulative and differential mass loss traces were used to quantify the amount of CH present in the system; towards this, well-established methods detailed in prior studies [40, 41] were used.

3 Phase boundary nucleation and growth model

A modified pBNG model is applied to describe the influence of PCE on early-age hydration kinetics of C_3S. Akin to classical pBNG models applied to cementitious systems [3, 7, 8, 42–45], the model used herein assumes that a single product of constant density forms heterogeneously on solid-phase substrate boundaries (i.e., C_3S particles' surfaces) at a given nucleation event (i.e., at time = τ h), and assumes that its subsequent growth drives and controls—as the rate controlling mechanism—the kinetics of C_3S hydration. This assumption—typically termed as *site saturation*—entails that after the initial burst of nucleation, no further nuclei of the product form. As per these criteria, the volume fraction of the product within the paste [$X(t)$, unitless] is given by Eq. 11 [1, 25, 33, 35, 42, 46].

$$X(t) = 1 - exp\left[-2k_G \cdot (t - \tau) \cdot \left(1 - \frac{F_D[k_s \cdot (t - \tau)]}{k_s \cdot (t - \tau)}\right)\right]$$
(1)

$$\text{where, } F_D(x) = exp(-x^2) \int_0^x exp(y^2)\,dy$$
(2)

$$k_s = G_{out}(t) \cdot \left(\pi \cdot g \cdot l_{density} \right)^{\frac{1}{2}} \tag{3}$$

$$g = \left[\frac{G_{par}(t)}{G_{out}(t)} \right]^2 \tag{4}$$

$$k_G = r_G \cdot G_{out}(t).a_{BV} \tag{5}$$

In Eq. 1, F_D represents the f-Dawson function shown as the integral in Eq. 2. The parameter k_s (h^{-1}) represents the inverse of time needed by the product to completely cover the surface of the anhydrous C_3S particles [7, 42] (Eq. 3). Its value depends on the nucleation density of the product ($l_{density}$, μm^{-2}), that is, the number of product nuclei per unit surface area of C_3S particulates, as well as the product's growth rate and geometry. In this study, it is assumed that the growth of the product occurs in an anisotropic manner, while varying with respect to time. The growth rates in the outward (i.e., normal to and away from C_3S particles' surface) and lateral (i.e., parallel to the C_3S particles' surface boundary) directions are represented as $G_{out}(t)$ and $G_{par}(t)$, respectively. Along the two-dimensional plane parallel to the C_3S surface, $G_{par}(t)$ is assumed to be isotropic [7, 25, 33]. It is worth noting that such temporal variation of the product growth rate is a departure from classical pBNG models—wherein, throughout the entire duration of hydration, the growth rate is assumed to remain constant. This implementation of variable product growth rate—based on the original study of Bullard et al. [46], and subsequently adopted by several researchers [11, 25, 33, 35]—captures sharp changes in C–S–H's growth rate as its supersaturation in the solution varies in a highly nonlinear fashion with time. While G_{out} and G_{par} vary with time, a ratio of 1:0.50 for G_{out}:G_{par} is maintained; as such, the anisotropy factor [i.e., g (unitless), shown in Eq. 4] of the product nuclei, remains constant at 0.25 throughout the entirety of C_3S hydration measured via microcalorimetry. This relationship between G_{out} and G_{par} causes the product to acquire aspherical geometry [7, 42]—essentially mimicking fiber-like geometry of C–S–H observed experimentally at early ages [47, 48].

In Eq. 1, the parameter k_G (h^{-1}) represents the inverse of time required for occupation of the capillary pore volume by the product. k_G is a function of G_{out}, and another constant r_G (unitless); here, r_G (Eq. 5) represents the ratio of product growth rate into vis-à-vis out of the substrate in the direction normal to the substrate. In previous studies [7, 42], focused on early age hydration of cement (and C_3S), it has been reported that hydrates do not penetrate the anhydrous particles, and, therefore, $r_G \approx 0.50$. As simulations presented in the current study pertain to early ages, the value of r_G is assumed to be constant at 0.50. The value of k_G, and thus kinetics of C_3S hydration, also

depend on the boundary area of the substrate per unit volume of the paste (a_{BV}, μm^{-1}) (Eq. 6). The paste's volume is simply the initial cumulative volume of the paste (i.e., volumes of C_3S and water), and the substrate's area is the initial surface area of C_3S particles that is available for nucleation of product. In Eq. 6, SSA_{C_3S} (units of $m^2\ kg^{-1}$) is the specific surface area of C_3S particles, ρ_W is the density of water (i.e., 1000 $kg\ m^{-3}$) and ρ_{C_3S} is the density of C_3S (i.e., 3150 $kg\ m^{-3}$). By combining SSA_{C_3S} and $l_{density}$, the total number of supercritical product nuclei (N_{nuc}, unit of g_{C3S}^{-1}) produced per gram of C_3S can be calculated [33, 43, 45, 49] (Eq. 7).

$$a_{BV} = \left[\frac{SSA_{C_3S}}{\left\{ \frac{\frac{l}{s}}{\rho_W} + \frac{1}{\rho_{C_3S}} \right\}} \right] \tag{6}$$

$$N_{nuc} = SSA_{C3S} \cdot l_{density} \tag{7}$$

The fraction of the paste' volume occupied by the product [$X(t)$], as calculated from Eq. 1, and the degree of hydration (a) of C_3S are linked by yet another constant, B (unitless) [25, 35, 46], as shown in Eqs. 8–9:

$$\alpha(t) = B \cdot X(t) \tag{8}$$

$$B = \left[\left(\frac{\frac{\rho_{C_3S}}{\rho_{products}}}{\frac{l \cdot \rho_{C_3S}}{\rho_{water}} + 1} \right) \left(\frac{c + \frac{1}{\rho_{C_3S}} - \frac{1}{\rho_{water}}}{\frac{1}{\rho_{product}} - \frac{1}{\rho_{water}}} \right) \right]^{-1} \tag{9}$$

where, $\rho_{product}$ is the average wet density of hydrates (assumed to be 2070 $kg\ m^{-3}$, based on the stoichiometric ratio of formation and individual densities of the two hydrates, C–S–H and CH) [50, 51], and the parameter $c = -7.04 \times 10^{-5}\ m^3\ kg^{-1}$ stands for the chemical shrinkage of the paste that occurs when 1 kg of C_3S is fully hydrated [35, 46, 52].

Based on the above equations (i.e., Eqs. 1–9), to numerically reproduce the experimentally-derived reaction rates, the variables that need to be ascertained are: $G_{out}(t)$ and $l_{density}$. Of these two variables, $G_{out}(t)$ is a function of time, whereas $l_{density}$ is constant (with respect to time). For a given system, to determine the optimum functional form of G_{out} and the optimum value of $l_{density}$ and, a Nelder–Mead based simplex algorithm [35, 53, 54], based on non-linear optimization and derivative-free routines, is implemented in two steps. In the first step, the value of G_{out} is kept constant at 0.075 $\mu m\ h^{-1}$—a value derived from microscopy-based analyses of early age C–S–H growth in C_3S and similar systems [47, 48, 55]. The algorithm varies the values of $l_{density}$ within predefined bounds (i.e.,
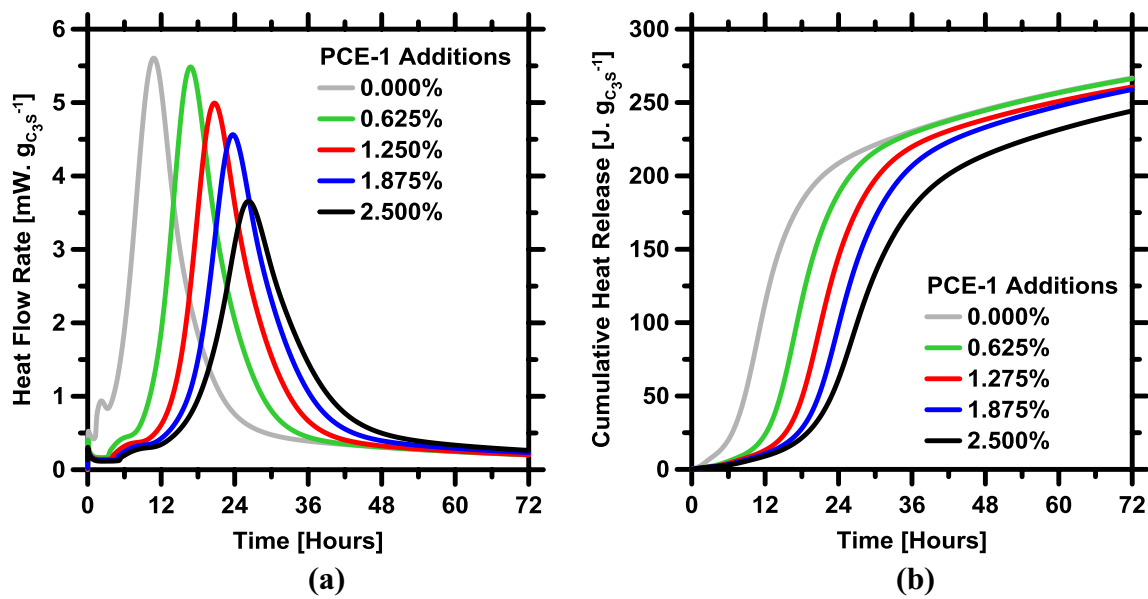
Fig. 2 Isothermal microcalorimetry based determinations of time-dependent **a** heat flow rate and **b** cumulative heat release of C_3S pastes provisioned with PCE-1 at different dosages (C_{PCE}). The l/s for pastes included in these figures, as well as the subsequent ones, is 0.45. The uncertainty in measured heat flow rate at the main hydration peak is $\pm 2\%$

0.01-to-100 µm h^{-1}) until the deviation between measured and simulated rates of reaction (*da/dt*) is minimized. It is worth highlighting that up to the first simulation step, the model represents the conventional pBNG formulation [8]—wherein the anisotropic growth of product, several nuclei of which precipitate at a virtual time τ (h), is assumed to be constant. To factor in the temporal variation in product growth rate, the second and final simulation step is employed. In this step, at a given time *t*, the optimum value of $I_{density}$, determined from the first step, is used as constant, whereas G_{out} is iteratively varied between 10^{-3} and 10^3 µm h^{-1}. At convergence, that is, when the deviation between the simulated and measured reaction rates reaches its minimum (i.e., within 0.05%), the value of G_{out} yielded by the optimization process is finalized as the optimum. By implementing the optimization process over 72 h (or longer for PCE-3 containing pastes) of hydration, using a time step of 0.01 h, the optimum values of G_{out} for the entire duration of C_3S hydration are thus determined. The functional form of G_{out}, obtained from the optimization routine, mimics the product's non-monotonic and nonlinear evolution of growth rate as a function of its supersaturation in the solution. In prior publications [11, 25, 33, 35, 46], which employ similar simulation scheme, it has been shown that such functional form of the product growth rate—as obtained from the simulations—reproduced the intrinsic changes in the evolution of the solution's chemistry (e.g., changes in pH, ionic strength, and water activity). Therefore, whereas this scheme of deriving the functional form of the product growth rate is indirect, the final results

are still reflective of the physical processes occurring in the system [11, 35, 46, 48, 55].

4 Results and discussion

Figure 2 shows representative heat evolution profiles of C_3S pastes provisioned with PCE-1 at different dosages (i.e., 0–2.5%).

As can be seen, PCE significantly suppresses C_3S hydration rates, as marked by various characteristic aspects of the pastes' heat evolution profiles: lengthening of the induction period (the period between the initial wetting peak and the onset of acceleration), rightward shift of the heat evolution curves, and reduced heat flow rates at the main hydration peak. The suppression of hydration induced by PCE increases monotonically with its dosage, which entails good correlation between amount of PCE present in the paste and the resultant reduction of C_3S hydration rates. This correlation is indicative of inhibition of C_3S dissolution sites (thus causing prolongation of the induction period), and C–S–H nucleation sites (thus causing slower approach to the main hydration peak)—both of which most likely manifest as a result of adsorption of PCE molecules on C_3S particles' surfaces, and scale with PCE dosage [19, 22–25]. It is worth pointing out that provision of PCE in the paste retards not only the approach to the main hydration peak but also the departure from it (i.e., slightly lower slope of the deceleration regime, as shown in Fig. 2a). Slower post-peak deceleration in [C_3S + PCE]
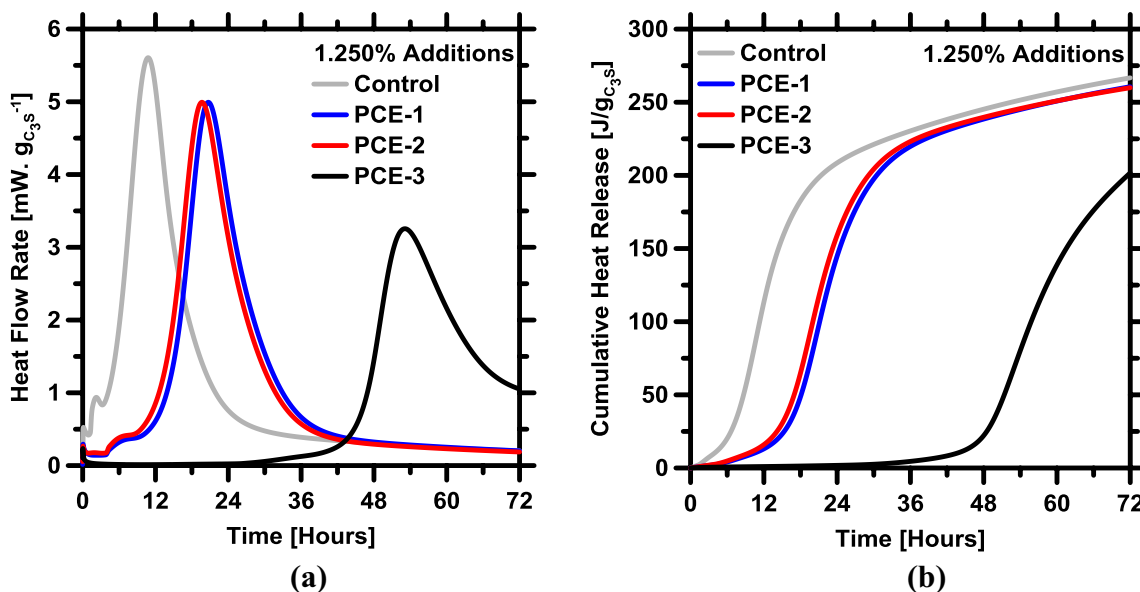
Fig. 3 Isothermal microcalorimetry based determinations of time-dependent **a** heat flow rate and **b** cumulative heat release of C_3S pastes provisioned with different PCEs (i.e., PCE-1, PCE-2, and PCE-3) at equivalent dosage (C_{PCE}) of 1.25%

pastes implies that, at later ages, the rate of hydration of C_3S in such pastes is relatively faster than in the control system (i.e., [C_3S + 0% PCE] paste); as such, much of the loss in early-age reactivity, that is induced by PCE, is recouped at later ages. This is better shown in Fig. 2b, wherein, at later ages (i.e., ≈ 72 h), the cumulative heat release of [C_3S + PCE] pastes converge—or, appear to be on track to converge—with that of the control system.

Results shown in Fig. 2, and the above discussion, describe the role of PCE dosage on C_3S hydration rates. To better understand the effects of PCE's molecular architecture on C_3S hydration kinetics, heat evolution profiles of [C_3S + PCE] pastes, prepared with equivalent dosages but different types of PCE, were compared (Fig. 3).

It is evident that regardless of the molecular architecture, all three PCEs suppress C_3S hydration at early ages (Fig. 3a). In addition to the pre-peak suppression of hydration (e.g., slower approach to the main hydration peak), the slower deceleration beyond the main hydration peak is common among the three PCEs. The slower deceleration results in convergence (or, in case of PCE-3, a trajectory that would eventually result in convergence) of cumulative heat release at later ages. While, qualitatively, the general nature of hydration suppression is similar amongst the three PCEs, there are substantial differences in the magnitude of such decelerations. As can be seen in Fig. 3, C_3S hydration is more significantly suppressed by PCE-3 as compared to PCE-1 and PCE-2; the
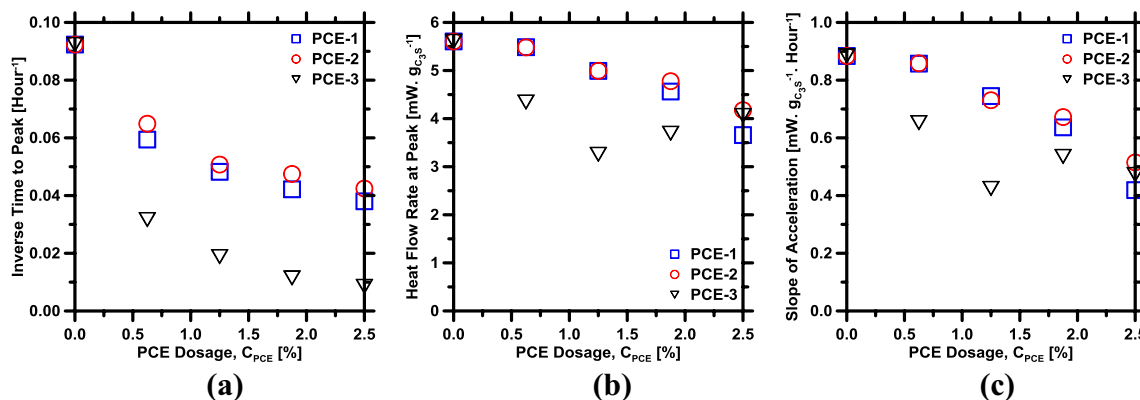

Fig. 4 The calorimetric parameters: **a** inverse of time to the main hydration peak, **b** heat flow rate at the main hydration peak, and **c** slope of the acceleration regime, extracted from heat evolution profiles, and plotted against PCE dosage. For a given system, the uncertainty in each calorimetric parameter is ± 2%

latter two produce similar magnitudes of suppression. Although the results shown in Fig. 3 pertain to a single PCE dosage (i.e., 1.25%), the stark difference—between the magnitude of suppression of C_3S hydration induced by PCE-3 vis-à-vis those by PCE-1 and PCE-2—was also observed at other dosages. Since all PCEs belong to the same polymer family (i.e., same composition of backbone and side chains), it is clear that the differences (or similarities) in their potential to suppress C_3S hydration arise due to intrinsic differences (or similarities) in their molecular architecture. Such architectural differences are expected to dictate their adsorption capacity, and, thus, their ability to inhibit sites of C_3S dissolution and C–S–H nucleation. As PCE-3 has the highest potential to suppress C_3S hydration, it can be said that its molecular architecture is more favorable towards adsorption on C_3S particles' surfaces. Along the same lines, as PCE-1 and PCE-2 produce equivalent suppressions of hydration at equivalent dosages, it is expected that their molecular architectures, and thus their adsorption potentials, are broadly similar. Further details pertaining to the role of PCE's molecular architecture on C_3S hydration suppression are discussed later in this section.

To better contrast suppression of C_3S hydration, as prompted by the three PCEs, characteristic calorimetric parameters [i.e., inverse of time corresponding to the main hydration peak (h^{-1}), heat flow rate at the main hydration peak ($mW\ g_{C3S}^{-1}$), and slope of the acceleration regime ($mW\ g_{C3S}^{-1}\ h^{-1}$)—indicative of acceleration or retardation in hydration kinetics [25, 33, 43, 56, 57]—were extracted and plotted against the PCE dosage (Fig. 4).

As can be seen, with increasing PCE dosage, the induction period's length increases (Fig. 2); this delays the incidence of the main hydration peak (Fig. 4a). This indicates that interactions between PCE and C_3S delay the hydrate nucleation event (i.e., massive precipitation of C–S–H and

CH, which occurs around the time when the induction period terminates) [2, 9, 25, 58]. These results are in good agreement with prior studies [17, 22, 24, 25], which have reported that the adsorption of PCE molecules on C_3S particles' surfaces blocks C_3S dissolution sites, which causes deceleration of C_3S dissolution and—as a consequence—prolongs the induction period. Akin to the trends in (inverse of) time of the main hydration peak, the other two calorimetric parameters—heat flow rate at the peak and slope of the acceleration regime—also decrease progressively with increasing amount of PCE in the paste (Fig. 4b, c). These results suggest that PCE not only delays the time of product nucleation but also suppresses the product's post-nucleation precipitation rate—as can also be seen in Figs. 2 and 3. Past literature [24, 25] suggests that such delay occurs due to interactions between PCE and C–S–H nuclei. More specifically, these studies [24, 25] suggest that PCE molecules (i.e., those that are not adsorbed on C_3S particles' surfaces and still remain in the solution) adsorb onto positively charged C–S–H surfaces, partially blocking their access to the contiguous solution, and, thus, diminishing their growth rate (and, hence, their precipitation rate). Furthermore, as PCE molecules remain adsorbed on C–S–H surfaces, the aforementioned inhibition of C–S–H's growth persists even at later stages of hydration. This is better revealed in Figs. 2a and 3a, wherein it is shown that the post-peak deceleration of [C_3S + PCE] paste is slower than in the control paste. Due to this, the cumulative heat release of [C_3S + PCE] pastes approach convergence with that of the control system at later ages (Figs. 2b, 3b).

The equivalency in calorimetric parameters of pastes prepared with PCE-1 and PCE-2 (Fig. 4) suggests that the hydration-suppression effects of the two PCEs are broadly similar. This equivalency is corroborated in Fig. 5, which shows that in [C_3S + PCE-1] and [C_3S + PCE-2] pastes—when prepared with equivalent dosage of PCE—the degree of
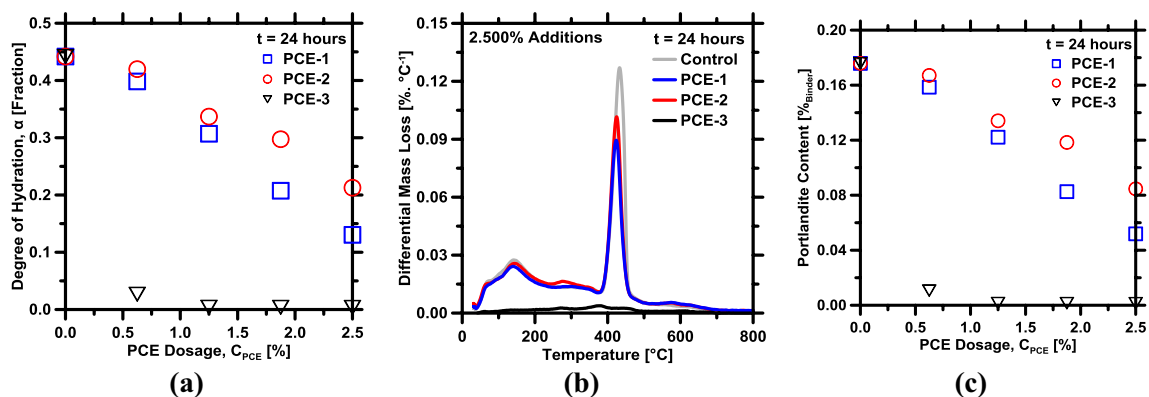

Fig. 5 a Isothermal microcalorimetry based determinations of time-dependent degree of reaction (α) of C_3S. **b** DTG traces showing differential mass loss profiles, and **c** mass contents of portlandite (CH: as %$_{mass}$ of the binder) as determined from analyses of DTG traces, in [C_3S + PCE] pastes at 24 h. The highest uncertainty in phase quantifications by DTG is ± 2.5%

hydration of C_3S (α) and portlandite (CH) contents at 24 h are similar. These results are not surprising because PCE-1 and PCE-2 have similar molecular architectures—with similar values of C/E, n, P, and M_w (see Table 1)—and, thus, are expected to have similar potentials to adsorb on silicate (i.e., C_3S and C–S–H) surfaces and similar capacities to block their access to the contiguous solution. Comparisons between PCE-1/PCE-2 and PCE-3 are, however, not trivial because of significant differences in their molecular architectures (Table 1). As can be seen in Fig. 5, at a given dosage, suppression of hydration induced by PCE-3 is considerably more severe (i.e., lower α and lower CH content at 24 h) as compared to those induced by PCE-1 and PCE-2. As the C/E of PCE-3 is significantly larger (i.e., $C/E = 5.20$) as compared to those of PCE-1 and PCE-2 (i.e., $C/E = 1.80$ and 2.10, respectively), it can be said that the lower side chain grafting density of PCE-3 permits a higher negative charge on the backbone, and, thus, improved adsorption onto positively charged silicate surfaces [15, 26–28]; this manifests as greater suppression of hydration in [C_3S + PCE-3] pastes. Furthermore, the length of the side chain (i.e., given by P) of PCE-3 is shorter (i.e., $P = 17$) than those of PCE-1 and PCE-2 (i.e., $P = 23$). As prior studies [17, 29] have indicated, smaller side chains ensure that access to the negative charges on the PCE's backbone is not hindered or limited by steric hindrance (induced by the side chains). This enables better adsorption of PCE molecules onto silicate surfaces, thus resulting in superior hydration inhibition. Lastly, on account of lower side chain grafting density, shorter side chain length, and smaller number of repeating units (i.e., n), the overall molecular weight of PCE-3 is lower (i.e., $M_w = 11,990$ g mol^{-1}) than PCE-1 and PCE-2 (i.e., $M_w = 25,145$ and $23,166$ g mol^{-1}). This entails that for a given (mass-based) dosage, the number of PCE-3 molecules in the paste is higher than those prepared with

PCE-1 or PCE-2. On account of their larger population in the paste, PCE-3 molecules are able to adsorb more effectively on C_3S and C–S–H surfaces, and, thus, suppress C_3S hydration to a greater extent as compared to the other two PCEs.

The discussion in the above paragraph provides a basis—albeit qualitative—for explaining the links between molecular architecture of PCE and its ability to suppress C_3S hydration. However, through such qualitative basis, it is impossible to quantify the superiority of a given PCE—in terms of inducing retardation of C_3S hydration kinetics—as compared to another PCE of a different molecular architecture. For example, while it is known that higher and lower values of C/E and P, respectively, cause superior suppression of C_3S hydration, such knowledge does not allow quantitative prediction of how much more retardation a PCE (say, with higher C/E and lower P compared to another PCE) will induce compared to another. In a recent paper, Marchon et al. [59] suggested that the net retardation of C_3S (or cement) hydration kinetics induced by PCE is proportional to: (1) the concentration of PCE molecules—expressed as the ratio of its dosage in paste (C_{PCE}: expressed as %$_{mass}$) to its molecular weight (M_w)—and (2) a function (f) of C/E, shown in Eq. 10. The former proportionality (i.e., with respect to PCE concentration) is expected because larger number of PCE molecules in the paste would entail greater probability of their adsorption on silicate (i.e., C_3S and C–S–H) surfaces, and, therefore, greater retardation. It is worth noting that PCE concentration inherently incorporates the effects of dosage and architectural parameters of PCE (i.e., n, P, C/E, and molecular weights of the side chain and backbone—as shown in Table 1 and described in [20, 22]), and, therefore, serves as an encompassing parameter on its own. The latter proportionality [i.e., with respect to $f(C/E)$] captures
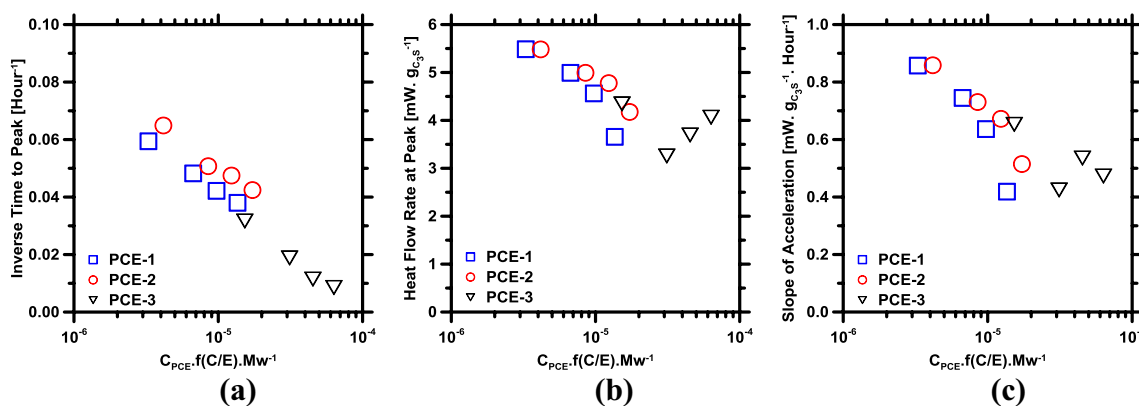

Fig. 6 The calorimetric parameters: **a** inverse of time to the main hydration peak, **b** heat flow rate at the main hydration peak, and **c** slope of the acceleration regime extracted from the calorimetry profiles, and plotted against the composite architectural parameter of the PCE (P_{PCE}: calculated using Eq. 11). The uncertainty in the value of P_{PCE} is on the order of $\pm 15\%$

the dependency of adsorption potential of PCE on the strength of electric field induced by its molecules on the adsorbent's surface. As described in prior publications [20, 59, 60], higher value of $f(C/E)$ implies greater magnitude, better exposure, and wider distribution of electric field induced by the PCE, and, therefore, better adsorption of its negatively charged backbone on the positively charged silicate surfaces. Marchon et al. [59] proposed that the overall retardation of C_3S (or cement) hydration kinetics, as induced by a given PCE, could be quantified by consolidating the aforementioned proportionalities into a composite architectural parameter (P_{PCE}: expressed in arbitrary units), as shown in Eq. 11. It must be noted that Marchon et al. [59] originally defined P_{PCE} using the molar mass of the repeating unit in the denominator. However, in Eq. 11, the molecular weight of (M_w) the entire PCE molecule is used (instead of just the repeating unit) in order to account for the PCE's backbone's length in addition to other architectural features. In Eq. 11, the variables (i.e., c_{PCE}, C/E and M_w) are expressed in their typical units as described in the Experimental Section.

$$f(C/E) = \left(\frac{C/E}{C/E + 1} \right)^{\frac{3}{2}} \qquad (10)$$

Composite Architectural Parameter $\left(P_{PCE} \right)$

$$= \frac{c_{PCE}}{M_w} f(C/E) = \frac{c_{PCE}}{M_w} \left(\frac{C/E}{C/E + 1} \right)^{\frac{3}{2}} \qquad (11)$$

To test the efficacy of Eq. 11, in terms of predicting the retardation caused by PCE, the calorimetric parameters—which capture alterations in C_3S hydration kinetics (as shown in Fig. 4)—were plotted against the composite architectural parameter (P_{PCE}) of PCE. As can be seen in Fig. 6, in spite of substantial differences in dosages and molecular architectures of PCEs, each calorimetric

parameter—extracted from heat evolution profiles of different pastes—converges, broadly, into a unified master trend.

Admittedly, the datapoints of two of the calorimetric parameters, that is, peak heat flow rate (Fig. 6b) and slope of the acceleration regime (Fig. 6c), are not as convergent as in the case of inverse of time to peak (Fig. 6a). These minor deviations—from the unified master trend—can be attributed to errors associated with the experimentally-determined parameters (e.g., PCE architectural parameters such as C/E, and calorimetric parameters). In spite of the aforementioned deviations, in general, it can be said that the deceleration of C_3S hydration kinetics increases, broadly in a logarithmic manner, with respect to increasing values of the composite architectural parameter (P_{PCE}) of PCE. This correlation suggests that Eq. 11 can be used as a robust, quantitative basis to compare and rank PCEs on the basis of their potential to suppress C_3S hydration rates. Equation 11 also allows prediction of additional (or reduction in) retardation—with respect to a benchmark system—if the PCE's dosage or molecular architecture are altered. As an example, if retardation of C_3S hydration caused by a given PCE is measured (e.g., using calorimetry), additional retardation at a higher dosage of the same PCE (or, a different PCE) can be readily predicted by plugging in the PCE dosage (or, architectural parameters) in Eq. 11.

The experimental results discussed thus far shed light on the effects of PCE dosage and molecular architecture on the overall hydration kinetics of C_3S. To better understand such effects, specifically in the context of alterations in nucleation and growth of the main hydrate (i.e., C–S–H), the pBNG model was applied. Figure 7 shows the simulated reaction rates of pastes compared against those obtained from experiments.

As can be seen, through optimization of the outward growth rate of the product [$G_{out}(t)$] and the product
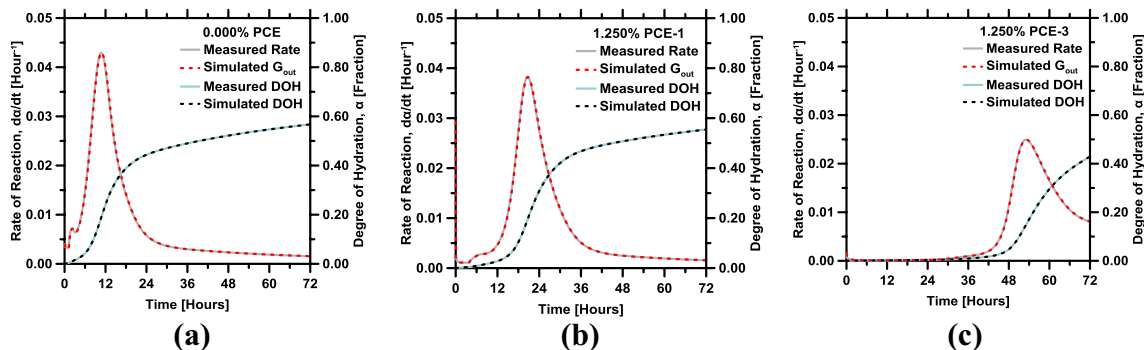

Fig. 7 Representative set of simulated and measured reaction rates (dα/dt; primary y-axis) and degree of reaction (α; secondary y-axis) for C_3S pastes prepared with varying PCE architectures and dosages of: **a** 0.000% PCE, **b** 1.250% PCE-1, and **c** 1.250% PCE-3. Simulations are deterministic, and, therefore, there is no uncertainty associated with them
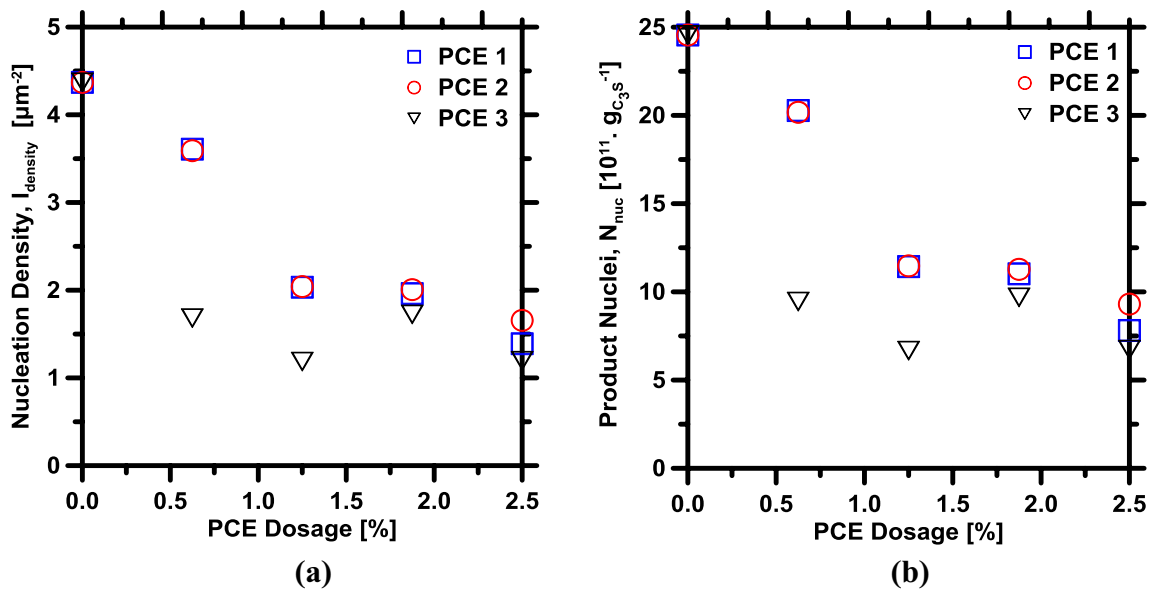
Fig. 8 Parameters derived from pBNG simulations: **a** nucleation density of the product ($I_{density}$), and **b** total number of super product nuclei formed per gram of C_3S (N_{nuc}: calculated from Eq. 7), plotted against PCE dosage (C_{PCE}). Simulations are deterministic, and, therefore, there is no uncertainty associated with them
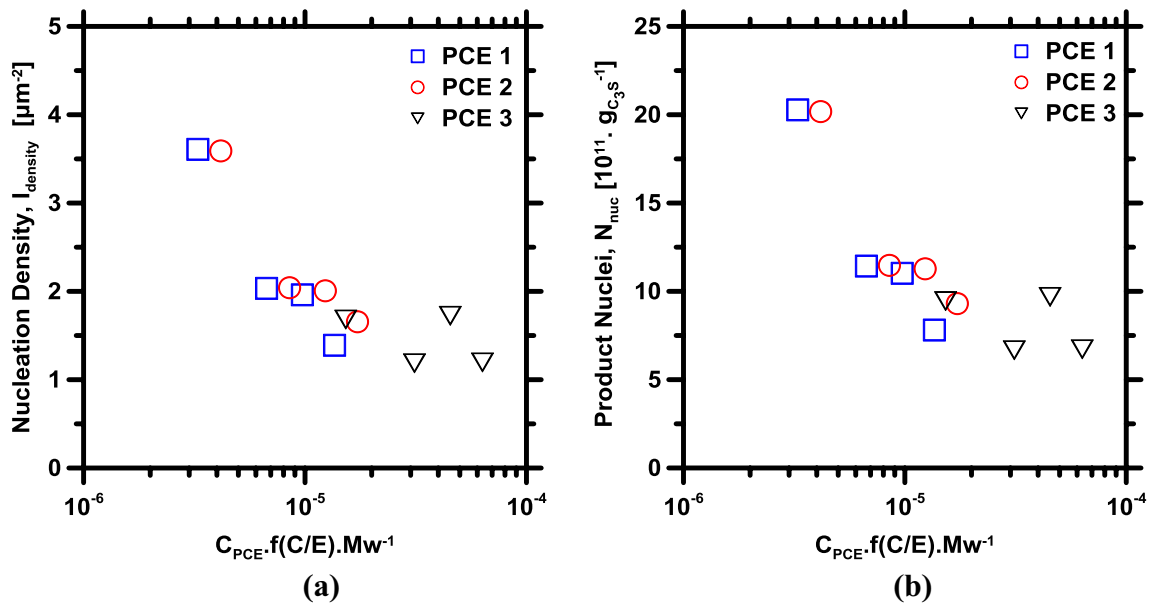

Fig. 9 Parameters derived from pBNG simulations: **a** nucleation density of the product ($I_{density}$), and **b** total number of super product nuclei formed per gram of C_3S (N_{nuc}), plotted against the composite architectural parameter of PCE (P_{PCE}: calculated from Eq. 11)

nucleation density ($I_{density}$), the experimental results are well reproduced by the model. Variations in these simulation parameters are investigated below to delineate the mechanistic origins of modifications in the nucleation and growth process in relation to PCE's molecular architecture and dosage.

Based on optimization of parameters by the pBNG model, it was found that PCE has profound effect on the hydrate nucleation event, which occurs at early ages, that is, in proximity to the time of termination of the induction period. As can be seen in Fig. 8a, the product nucleation density decreases monotonically with increasing PCE dosage. This manifests as a progressive
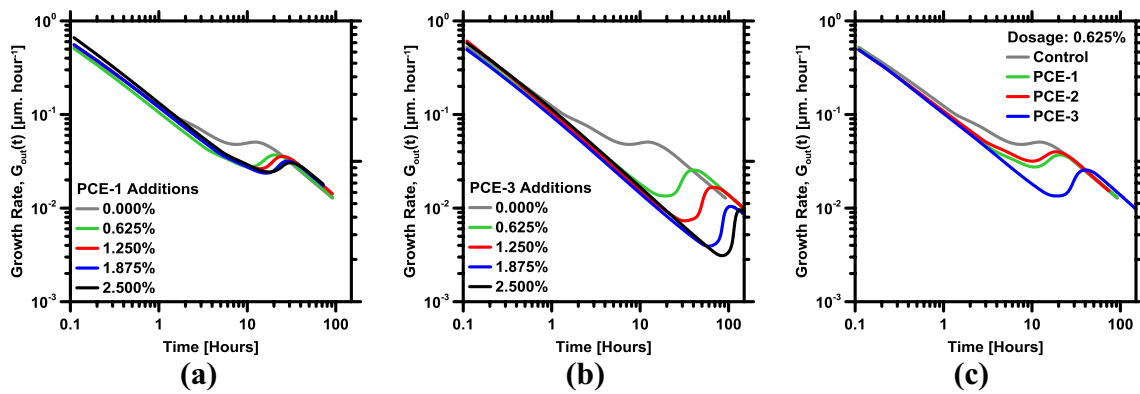
Fig. 10 The temporal evolution of outward growth rate of the product (G_{out}), as obtained from pBNG simulations, for: **a** pastes prepared with PCE-1 at different dosages, **b** pastes prepared with PCE-3 at different dosages, and **c** pastes prepared with differ-ent PCEs at a fixed dosage of 0.625%. Simulations parameters are deterministic, and, therefore, there is no uncertainty associated with them

decline in the number of supercritical product nuclei (N_{nuc}: calculated from Eq. 7)—forming heterogeneously on C_3S surfaces—with respect to increasing PCE dosage (Fig. 8b). These results corroborate the hypotheses presented above, as well as those advanced in previous studies [24, 25]—that adsorption of PCE molecules on C_3S surfaces inhibits topographical sites of C–S–H nucleation. As would be expected, at higher PCE dosages, larger fraction of C_3S particles' surface is blocked, and, thus, a greater number of C–S–H nucleation sites are inhibited. It is interesting to note that at any given dosage, PCE-3 results in lower product nucleation density (Fig. 8a)—and, therefore, smaller number of product nuclei (Fig. 8b)—as compared to the other two PCEs.

These results are in very good agreement with the trends derived directly from the experiments (Fig. 4), and suggest that the adsorption capacity—and, therefore, the potential to suppress C–S–H nucleation (and C_3S hydration)—of PCE-3 is superior. As stated previously, the superior retardation induced by PCE-3 can be attributed to its intrinsic molecular architecture [namely, lower side chain grafting density (i.e., higher *C/E*), smaller side chain length (i.e., lower *P*), and lower molecular weight (i.e., M_w)]—which enables better adsorption of its molecules onto C_3S surfaces, and, therefore, more effective blocking of topographical C–S–H nucleation sites.

Earlier in this section, it was shown that the composite architectural parameter of PCE (P_{PCE}: calculated using
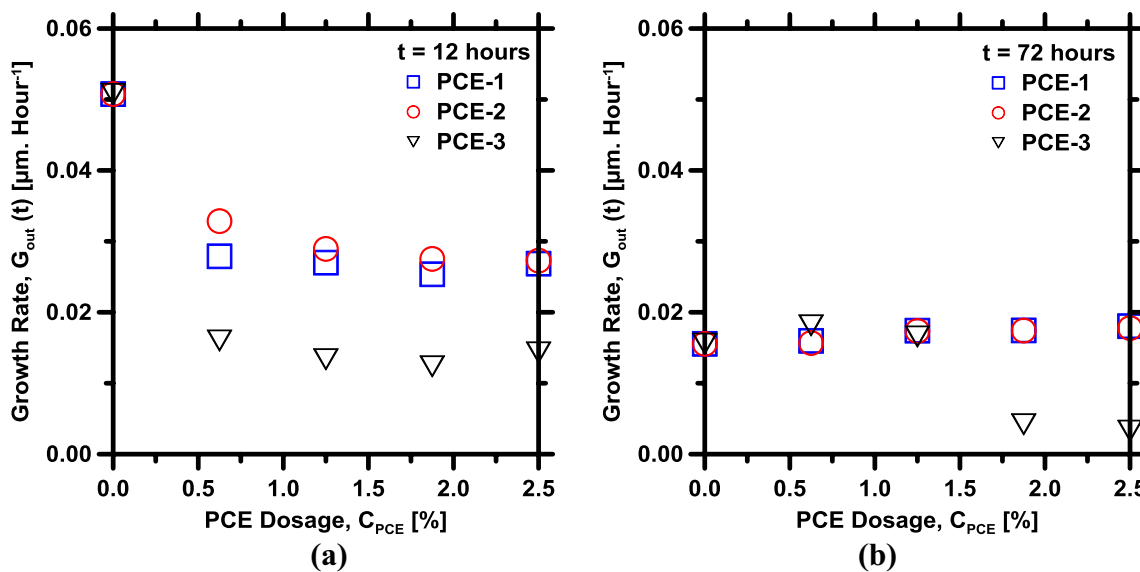

Fig. 11 The outward growth rate of the product, as obtained from pBNG simulations, at **a** t = 12 h, and **b** t = 72 h

Eq. 11) correlated very well with the resultant effect on C_3S hydration (Fig. 5). To further verify the applicability of the composite parameter—in terms of capturing the combined effects of PCE dosage and molecular architecture—the product nucleation density and the number of product nuclei were plotted against P_{PCE}. As can be seen in Fig. 9, akin to the calorimetric parameters (Fig. 5), each pBNG parameter (i.e., $I_{density}$ and N_{nuc}) converges onto a unified master trend; wherein, with increasing dosages of P_{PCE}, both $I_{density}$ and N_{nuc} decrease monotonically.

It is clarified that the master trends, which emerge in Fig. 9, are not devoid of deviations. These deviations are, however, minor, and can be attributed to the statistical variance in the experimentally-derived parameters (e.g., C/E of PCE). Notwithstanding, these results—in conjunction with those shown in Fig. 5—provide compelling evidence that the composite architectural parameter of PCE (P_{PCE}) is a reliable, and more importantly, a readily quantifiable indicator of the PCE's potential to suppress C_3S hydration.

Finally, the product's outward growth rate [$G_{out}(t)$], as obtained from pBNG simulations, are shown in Fig. 10.

As can be seen, G_{out} decreases by about three orders of magnitude—while evolving in a highly nonlinear manner with respect to time—over the course of C_3S hydration. Such temporal evolution of the growth rate has been reported [25, 33, 35, 46] to mimic the time-dependent evolution of C–S–H supersaturation in the solution. It is noted that at any given time, G_{out}—particularly between ages of 1 h and 24 h—is lower at higher PCE dosages (Fig. 10a).

Also, at equivalent dosages, G_{out} is lower in pastes prepared with PCE-3 as compared to those prepared with PCE-1 and PCE-2. To better contrast the influence of the different PCEs, values of G_{out} were extracted at different times, i.e., at 12 h (early age), and at t = 72 h (later age), and, ultimately, plotted against the PCE dosage. As can be seen in Fig. 11a, at early ages, G_{out} in [C_3S + PCE] pastes is consistently lower than in control pastes. This corroborates the hypothesis made earlier in this section—that the excess PCE molecules in the solution (that do not adsorb onto C_3S particles' surfaces) adsorb onto C–S–H nuclei, and, subsequently, block their access to the adjacent solution, thus inhibiting their growth rate [24, 25]. At any given PCE dosage, lower values of G_{out} in [C_3S + PCE-3] pastes, as compared to those prepared with other two PCEs, can be attributed to higher adsorption capacity of PCE-3 (i.e., on account of its molecular architecture), as has been explained previously in this section and highlighted in Figs. 4 and 8. At later ages, that is, at t = 72 h (Fig. 11b), the variations in G_{out} with respect to PCE's dosage and molecular architecture are significantly less pronounced. This is attributed to depletion of C–S–H supersaturation in the solution—which, in turn, causes G_{out} to diminish [11, 24, 25, 33] and converge to similar values, regardless of dosage or molecular architecture of the PCE in the paste.

By and large, the results described so far support the theory that hydration of C_3S is suppressed by PCE—wherein, adsorption of PCE molecules onto C_3S surfaces suppresses C_3S dissolution and C–S–H nucleation. The adsorption of PCE molecules onto C–S–H surfaces
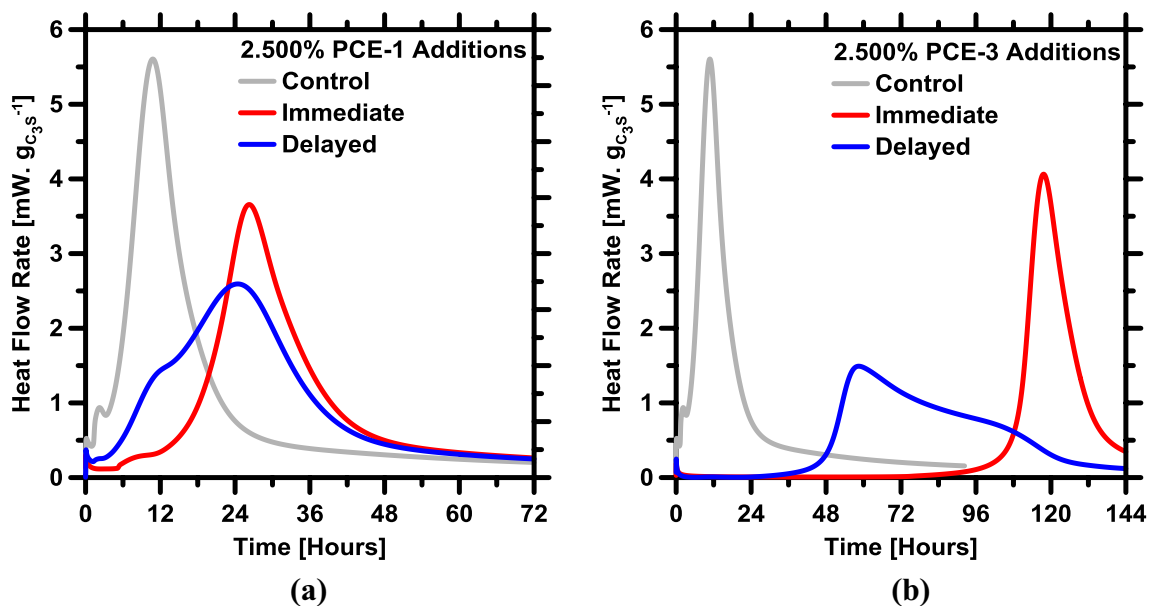

Fig. 12 Measured heat flow rates of [C_3S + 2.5% PCE] pastes, prepared with **a** PCE-1, and **b** PCE-3. Results corresponding to both immediate and delayed (i.e., by 5-min) addition of PCE are shown. For comparison, the control system with no PCE is also shown

suppresses the post-nucleation growth of C–S–H. Based on this theory, it is hypothesized that if the adsorption of PCE onto C_3S surfaces is reduced, the overall impact on inhibition of C_3S dissolution and C–S–H nucleation sites would consequently be reduced. To test this hypothesis, additional experiments were conducted, wherein PCE was incorporated into the paste in delayed mode (i.e., addition of PCE five mins after mixing of C_3S and DI-water). As can be seen in Fig. 12, when the addition of PCE is delayed, its impact on dissolution and nucleation site inhibition are indeed marginalized (albeit, not nullified). This manifests as shorter induction period and faster incidence of the main hydration peak compared to those in pastes provisioned with PCE at the time of mixing. Notwithstanding, in the case of delayed addition, the adsorption of PCE molecules onto surfaces of C–S–H—that form prior to, as well as after, the addition of PCE—results in substantial inhibition of its post-nucleation growth. This manifests as slower approach to and departure from the main hydration peak. It is also worth noting that in the case of delayed addition, as PCE molecules predominantly adsorb onto C–S–H surfaces (as opposed to C_3S and C–S–H surfaces), the suppression of post-nucleation growth of C–S–H (and, therefore, C_3S hydration) is more profound compared to pastes in which PCE is added at the time of mixing (Fig. 12). The results shown in Fig. 12, and the mechanisms described above, are in good agreement with prior studies [24, 59].

5 Conclusions

A hierarchical sequence of experiments and pBNG simulations were employed to elucidate the effects of comb-shaped polycarboxylate ether (PCE) polymer on hydration mechanisms of tricalcium silicate (C_3S). Emphasis was given to describe contributions of dosage and molecular architecture of PCE on early hydration of C_3S.

Results clearly show that hydration of C_3S is suppressed in presence of PCE—wherein, the deceleration scales with PCE content in the paste. The origin of such deceleration was hypothesized to be linked to the adsorption of PCE molecules on C_3S particles' surfaces, which inhibits topographical dissolution and C–S–H nucleation sites, and results in prolongation of the induction period. Furthermore, results suggest that adsorption of PCE molecules onto surfaces of C–S–H results in suppression of its post-nucleation growth long after termination of the induction period. This results in a slower approach to, as well as departure from, the main hydration peak.

Through rigorous analyses of decelerating effects induced by three different PCEs, this study develops a robust correlation between the molecular architecture of

PCE and its potential to suppress C_3S hydration. Results show that PCEs with lower side chain grafting density (i.e., higher C/E: carboxylate-to-ether ratio), smaller side chain length (i.e., smaller P: number of monomers per side chain), and lower overall molecular weight have greater potential to adsorb on silicate surfaces, and, therefore, suppress C_3S hydration. By consolidating results pertaining to the three different PCEs, the study advances a simple numerical equation—which unifies the PCE's dosage and architectural parameters into a single numerical value—to assess, in a quantitative manner, a given PCE's potential to suppress C_3S hydration.

Overall, outcomes of this study provide novel mechanistic insights into the root-cause of decelerating effects of PCE. The discussion provides an improved understanding of how the dosage and architectural parameters of PCE—which can readily be characterized using conventional experimental techniques—affect the hydration of C_3S at early ages. Such knowledge is expected to aid in uncovering the underlying mechanisms that describe the influence of PCE on the hydration of other cementitious phases (e.g., C_3A), as well as the development of fresh- (e.g., rheology) and hardened-properties (e.g., compressive strength) of cementitious systems.

Data availability The raw/processed data required to reproduce the findings presented in the paper is available upon request.

Compliance with ethical standards

Conflict of interest The authors declare that they have no competing interests.

References

1. Taylor HF (1997) Cement chemistry. Thomas Telford, London
2. Bullard JW, Jennings HM, Livingston RA, Nonat A, Scherer GW, Schweitzer JS, Scrivener KL, Thomas JJ (2011) Mechanisms of cement hydration. Cem Concr Res 41(12):1208–1223
3. Thomas JJ, Jennings HM, Chen JJ (2009) Influence of nucleation seeding on the hydration mechanisms of tricalcium silicate and cement. J Phys Chem C 113(11):4327–4334
4. Masoero E, Del Gado E, Pellenq R-M, Ulm F-J, Yip S (2012) Nanostructure and nanomechanics of cement: polydisperse colloidal packing. Phys Rev Lett 109(15):155503
5. Yu P, Kirkpatrick RJ, Poe B, McMillan PF, Cong X (1999) Structure of calcium silicate hydrate (C–S–H): near-, mid-, and far-infrared spectroscopy. J Am Ceram Soc 82(3):742–748

6. Abdolhosseini Qomi MJ, Ulm F-J, Pellenq RJ-M (2012) Evidence on the dual nature of aluminum in the calcium–silicate–hydrates based on atomistic simulations. J Am Ceram Soc 95(3):1128–1137

7. Scherer GW, Zhang J, Thomas JJ (2012) Nucleation and growth models for hydration of cement. Cem Concr Res 42(7):982–993

8. Thomas JJ (2007) A new approach to modeling the nucleation and growth kinetics of tricalcium silicate hydration. J Am Ceram Soc 90(10):3282–3288

9. Kumar A, Bishnoi S, Scrivener KL (2012) Modelling early age hydration kinetics of alite. Cem Concr Res 42(7):903–918

10. Thomas JJ, Biernacki JJ, Bullard JW, Bishnoi S, Dolado JS, Scherer GW, Luttge A (2011) Modeling and simulation of cement hydration kinetics and microstructure development. Cem Concr Res 41(12):1257–1278

11. Ley-Hernandez AM, Lapeyre J, Cook R, Kumar A, Feys D (2018) Elucidating the effect of water-to-cement ratio on the hydration mechanisms of cement. ACS Omega 3(5):5092–5105

12. Mehdipour I, Kumar A, Khayat KH (2017) Rheology, hydration, and strength evolution of interground limestone cement containing PCE dispersant and high volume supplementary cementitious materials. Mater Des 127:54–66

13. Arora A, Aguayo M, Hansen H, Castro C, Federspiel E, Mobasher B, Neithalath N (2018) Microstructural packing-and rheology-based binder selection and characterization for ultra-high performance concrete (UHPC). Cem Concr Res 103:179–190

14. Cheung J, Jeknavorian A, Roberts L, Silva D (2011) Impact of admixtures on the hydration kinetics of portland cement. Cem Concr Res 41(12):1289–1309

15. Winnefeld F, Becker S, Pakusch J, Götz T (2007) Effects of the molecular architecture of comb-shaped superplasticizers on their performance in cementitious systems. Cem Concr Compos 29(4):251–262

16. Ridi F, Fratini E, Luciani P, Winnefeld F, Baglioni P (2012) Tricalcium silicate hydration reaction in the presence of comb-shaped superplasticizers: boundary nucleation and growth model applied to polymer-modified pastes. J Phys Chem C 116(20):10887–10895

17. Zingg A, Winnefeld F, Holzer L, Pakusch J, Becker S, Figi R, Gauckler L (2009) Interaction of polycarboxylate-based superplasticizers with cements containing different C3A amounts. Cem Concr Compos 31(3):153–162

18. Zingg A, Holzer L, Kaech A, Winnefeld F, Pakusch J, Becker S, Gauckler L (2008) The microstructure of dispersed and non-dispersed fresh cement pastes—new insight by cryo-microscopy. Cem Concr Res 38(4):522–529

19. Zingg A, Winnefeld F, Holzer L, Pakusch J, Becker S, Gauckler L (2008) Adsorption of polyelectrolytes and its influence on the rheology, zeta potential, and microstructure of various cement and hydrate phases. J Colloid Interface Sci 323(2):301–312

20. Gelardi G, Sanson N, Nagy G, Flatt RJ (2017) Characterization of comb-shaped copolymers by multidetection SEC, DLS and SANS. Polymers 9(2):61

21. Marchon D, Sulser U, Eberhardt A, Flatt RJ (2013) Molecular design of comb-shaped polycarboxylate dispersants for environmentally friendly concrete. Soft Matter 9(45):10719–10728

22. Marchon D, Juilland P, Gallucci E, Frunz L, Flatt RJ (2017) Molecular and submolecular scale effects of comb-copolymers on tri-calcium silicate reactivity: toward molecular design. J Am Ceram Soc 100(3):817–841

23. Artioli G, Valentini L, Voltolini M, Dalconi MC, Ferrari G, Russo V (2014) Direct imaging of nucleation mechanisms by synchrotron diffraction micro-tomography: superplasticizer-induced change of C–S–H nucleation in cement. Cryst Growth Des 15(1):20–23

24. Valentini L, Favero M, Dalconi MC, Russo V, Ferrari G, Artioli G (2016) Kinetic model of calcium–silicate hydrate nucleation and growth in the presence of PCE superplasticizers. Cryst Growth Des 16(2):646–654

25. Meng W, Lunkad P, Kumar A, Khayat K (2016) Influence of silica fume and polycarboxylate ether dispersant on hydration mechanisms of cement. J Phys Chem C 120(47):26814–26823

26. Kirby GH, Lewis JA (2004) Comb polymer architecture effects on the rheological property evolution of concentrated cement suspensions. J Am Ceram Soc 87(9):1643–1652

27. Sakai E, Kawakami A, Daimon M (2001) Dispersion mechanisms of comb-type superplasticizers containing grafted poly (ethylene oxide) chains. Macromol Symp Wiley Online Libr 175:367–376

28. Yamada K, Takahashi T, Ogawa S, Hanehara S (2000) Molecular structure of the polycarboxylate-type superplasticizer having tolerance to the effect of sulfate ion. Cem Concr Sci Technol 54:79–86

29. Yoshikawa J, Lewis JA, Chun B-W (2009) Comb polymer architecture, ionic strength, and particle size effects on the $BaTiO_3$ suspension stability. J Am Ceram Soc 92(s1):S42–S49

30. Ridi F, Dei L, Fratini E, Chen S-H, Baglioni P (2003) Hydration kinetics of tri-calcium silicate in the presence of superplasticizers. J Phys Chem B 107(4):1056–1061

31. Sowoidnich T, Rachowski T, Rößler C, Völkel A, Ludwig H-M (2015) Calcium complexation and cluster formation as principal modes of action of polymers used as superplasticizer in cement systems. Cem Concr Res 73:42–50

32. Yamada K, Ogawa S, Hanehara S (2001) Controlling of the adsorption and dispersing force of polycarboxylate-type superplasticizer by sulfate ion concentration in aqueous phase. Cem Concr Res 31(3):375–383

33. Lapeyre J, Kumar A (2018) Influence of pozzolanic additives on hydration mechanisms of tricalcium silicate. J Am Ceram Soc 101(8):3557–3574

34. Bazzoni A, Cantoni M, Scrivener KL (2014) Impact of annealing on the early hydration of tricalcium silicate. J Am Ceram Soc 97(2):584–591

35. Oey T, Kumar A, Falzone G, Huang J, Kennison S, Bauchy M, Neithalath N, Bullard JW, Sant G (2016) The influence of water activity on the hydration rate of tricalcium silicate. J Am Ceram Soc 99(7):2481–2492

36. Ferraris CF, Hackley VA, Avilés AI (2004) Measurement of particle size distribution in portland cement powder: analysis of ASTM round robin studies. Cem Concr Aggreg 26(2):71–81

37. Ferrari L, Bernard L, Deschner F, Kaufmann J, Winnefeld F, Plank J (2012) Characterization of polycarboxylate-ether based superplasticizer on cement clinker surfaces. J Am Ceram Soc 95(7):2189–2195

38. Agullo L, Toralles-Carbonari B, Gettu R, Aguado A (1999) Fluidity of cement pastes with mineral admixtures and superplasticizer—a study based on the marsh cone test. Mater Struct 32(7):479–485

39. Plank J, Zhimin D, Keller H, Hössle FV, Seidl W (2010) Fundamental mechanisms for polycarboxylate intercalation into C3A hydrate phases and the role of sulfate present in cement. Cem Concr Res 40(1):45–57

40. Zhang J, Scherer GW (2011) Comparison of methods for arresting hydration of cement. Cem Concr Res 41(10):1024–1036

41. Stoian J, Oey T, Bullard JW, Huang J, Kumar A, Balonis M, Terrill J, Neithalath N, Sant G (2015) New insights into the prehydration of cement and its mitigation. Cem Concr Res 70:94–103

42. Scherer GW (2012) Models of confined growth. Cem Concr Res 42(9):1252–1260

43. Oey T, Kumar A, Bullard JW, Neithalath N, Sant G (2013) The filler effect: the influence of filler content and surface area on cementitious reaction rates. J Am Ceram Soc 96(6):1978–1990

44. Garrault S, Nonat A (2001) Hydrated layer formation on tricalcium and dicalcium silicate surfaces: experimental study and numerical simulations. Langmuir 17(26):8131–8138

45. Puerta-Falla G, Kumar A, Gomez-Zamorano L, Bauchy M, Neithalath N, Sant G (2015) The influence of filler type and surface area on the hydration rates of calcium aluminate cement. Constr Build Mater 96:657–665

46. Bullard JW, Scherer GW, Thomas JJ (2015) Time dependent driving forces and the kinetics of tricalcium silicate hydration. Cem Concr Res 74:26–34

47. Bazzoni A, Ma S, Wang Q, Shen X, Cantoni M, Scrivener KL (2014) The effect of magnesium and zinc ions on the hydration kinetics of C_3S. J Am Ceram Soc 97(11):3684–3693

48. Scherer GW, Bellmann F (2018) Kinetic analysis of C–S–H growth on calcite. Cem Concr Res 103:226–235

49. Kumar A, Oey T, Kim S, Thomas D, Badran S, Li J, Fernandes F, Neithalath N, Sant G (2013) Simple methods to estimate the influence of limestone fillers on reaction and property evolution in cementitious materials. Cem Concr Compos 42:20–29

50. Allen AJ, Thomas JJ, Jennings HM (2007) Composition and density of nanoscale calcium–silicate–hydrate in cement. Nat Mater 6(4):311–316

51. Thomas JJ, Jennings HM, Allen AJ (2010) Relationships between composition and density of tobermorite, jennite, and nanoscale CaO–SiO_2–H_2O. J Phys Chem C 114(17):7594–7601

52. Bentz DP, Lura P, Roberts JW (2005) Mixture proportioning for internal curing. Concr Int 27(2):35–40

53. Nelder JA, Mead R (1965) A simplex method for function minimization. Comput J 7(4):308–313

54. McKinnon KI (1998) Convergence of the Nelder–Mead simplex method to a nonstationary point. SIAM J Optim 9(1):148–158

55. Bellmann F, Scherer GW (2018) Analysis of C–S–H growth rates in supersaturated conditions. Cem Concr Res 103:236–244

56. Berodier E, Scrivener K (2014) Understanding the filler effect on the nucleation and growth of C–S–H. J Am Ceram Soc 97(12):3764–3773

57. Bentz DP (2006) Modeling the influence of limestone filler on cement hydration using CEMHYD3D. Cem Concr Compos 28(2):124–129

58. Jennings HM (2008) Refinements to colloid model of CSH in cement: CM-II. Cem Concr Res 38(3):275–289

59. Marchon D, Juilland P, Gallucci E, Frunz L, Flatt R (2017) Molecular and submolecular scale effects of comb-copolymers on tricalcium silicate reactivity: toward molecular design. J Am Ceram Soc 100:817–841

60. Borukhov I (1998) Adsorption of polyelectrolytes and intercolloidal forces. Phys A Stat Mech Appl 249(1–4):315–320